applied sciences

MDPI

Article

Current Filaments in Asymmetric Surface Dielectric Barrier Discharge

Cecilia Piferi, Ruggero Barni, H. Eduardo Roman and Claudia Riccardi *

Dipartimento di Fisica, Università degli Studi di Milano-Bicocca, Piazza della Scienza 3, 20126 Milano, Italy; c.piferi@campus.unimib.it (C.P.); ruggero.barni@mib.infn.it (R.B.); eduardo.roman@mib.infn.it (H.E.R.)
* Correspondence: claudia.riccardi@unimib.it

Abstract: In this study, we examine the statistical properties of asymmetric surface dielectric barrier discharges (SDBD) produced by applying a periodic high voltage between two conducting displaced electrodes, located at the opposite sides of a flat dielectric panel. Here, the asymmetry refers to the fact that the lower electrode is fully covered with an insulating material, while the upper one, glued onto the dielectric surface, is otherwise left exposed to the air. Such a configuration allows the formation of a thin layer of plasma above the insulating surface. A single cycle signal consists of two well-separated half-cycle patterns, denoted as forward and backward strokes, corresponding to positive and negative voltages, respectively. They display a quite complex discharge pattern constituted by a sequence of individual peaks (bursts) of varying current and time duration. Specifically, we find that backward stroke bursts carry a positive mean charge $\langle Q \rangle \simeq 0.3$ nC and mean current $\langle I \rangle \simeq 35$ mA, with a mean duration $\langle \tau \rangle \simeq 15$ ns, while forward stroke bursts have a negative mean charge $\langle Q \rangle \simeq -0.1$ nC, a mean current $\langle I \rangle \simeq -20$ mA, and a mean duration $\langle \tau \rangle \simeq 11$ ns. The statistical analysis suggests that power injection can be tailored to produce the active agents in the plasma needed for a particular application. We also determined discharge spatial correlation patterns from measurements of the associated stimulated optical emission. The optical excitations occur as a result of the ionizing effect of the electromagnetic waves which ignite the discharge, followed by the electric current flow. In particular, we point out that one of the phases of the discharge is compatible with a cathode directed streamer phenomenon (backward stroke), while the mechanism acting for a forward stroke has a different structure.

Keywords: surface dielectric barrier discharge; atmospheric pressure non thermal plasma; streamer discharge

Citation: Piferi, C.; Barni, R.; Roman, H.E.; Riccardi, C. Current Filaments in Asymmetric Surface Dielectric Barrier Discharges. *Appl. Sci.* **2021**, *11*, 2079. https://doi.org/10.3390/app11052079

Received: 15 January 2021
Accepted: 20 February 2021
Published: 26 February 2021

1. Introduction

Dielectric barrier discharges (DBD) have found many industrial applications as ozone generators, plasma discharge panels, excimer lamps and in different types of surface modifications [1–5]. DBD are chracterized by the presence of an insulating material between the electrodes to prevent the occurrence of high electrical current arcs between them (arcing). They produce a non-thermal plasma at (or near) atmospheric pressure in the discharge gap region between electrodes (Figure 1a) [6,7].

The DBD geometry results in a quite uniform plasma distributed between electrodes, providing a large flow of activated or reactive compounds for the treatment of materials [8–10]. This technique enables the application of plasma processes at atmospheric pressure without a damaging heat load [11–15].

DBD have been used, for instance, to increase the wettability of polymers, to grow silicon oxide thin films, to perform sterilization by UV irradiation, and for air purification [16,17]. Variants of DBD are surface dielectric barrier discharges (SDBD) (Figure 1b), obtained by using a particular configuration of electrodes in direct contact with the dielectric material. To extend SDBD applications, asymmetrical electrode layouts (one isolated

and the other exposed to the air) were developed, in particular in the context of aerodynamics [18–21]. In the latter, the main purpose was the production of an ionic wind, flowing along the wing surface [22,23]. The resulting enhanced mixing of air flow and ionic wind was found to be beneficial for an active boundary layer control, pursuing drag reduction [24], lift enhancement [21], and stall prevention [25].

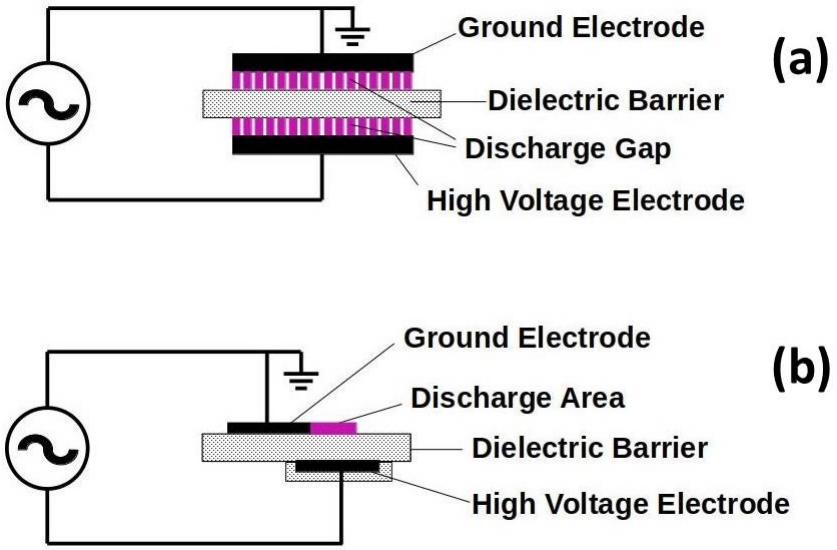

Figure 1. Schematic representations of: (**a**) dielectric barrier discharges (DBD), and (**b**) surface dielectric barrier discharges (SDBD). Discharges within the plasma are indicated in magenta colour.

In this work, we perform extensive statistical analysis of SDBD, complementing the study on DBD performed in [26], using an asymmetric device with an exposed (grounded) metal electrode, glued onto the dielectric surface, and a lower electrode covered by an insulating material (see Figure 1b). The purpose of our work is the characterization and the analysis of the mechanisms taking place during the discharge formation in SDBD, and its robustness when operating under steady state conditions. This is a basic requirement that a working plasma device should fulfil in order to be used in large-scale industrial applications. The study of SDBD properties are also interesting from a fundamental physics point of view, since they have not been thoroughly investigated, while DBD have not been thoroughly investigated either [6,26].

In the presence of high-voltage oscillating signals, SDBD display a complex pattern of electric discharges in the form of short bursts of activity, concentrated within each half-cycle of the wave signal period. They are often referred to as forward discharge or forward stroke (FS), and backward discharge or backward stroke (BS), depending on the sign of the applied voltage [27]. The two strokes are composed of a relatively large number of individual events, carrying electrical currents in the discharge area, for which the expression microdischarge was coined [6]. It is still not clear yet what the role played by FS and BS microdischarges is in the production of the induced airflow around the plasma [22,28,29].

At atmospheric pressure in air, SDBD operate in the so-called microdischarge regime, characterized by narrow current filaments with very short lifetimes (few tens of ns) [6,30]. Microdischarge filaments, or streamers, extend from the exposed electrode towards the dielectric surface above the covered electrode, more or less perpendicularly to the electrodes [30]. This spatial region roughly corresponds to the region where the electric field strength is at its maximum.

At a more fundamental level, it is not even clear if the discharge mechanism is the same during the two AC semi-cycles [30,31]. The origin of the differences between the two strokes may be due to the different asymmetries that, as a matter of fact, can be present in typical SDBD setups. The second, more general, source of asymmetry resides in the electrodes and

dielectric surface geometry, which induces electric field spatial non-uniformities, that can lead to differences between the two voltage polarities [22]. The alternating nature of the power supply, however, induces a subtle correlation between the two strokes, which are at work when the steady state operation regime is reached. Such correlations have been studied in DBD [26] by calculating the Hurst exponent of the corresponding random walk profiles [32,33], and we extend a similar study to SDBD.

In particular, further investigations are necessary by dealing with the mechanisms of microdischarge initiation at the restart of each one of the two strokes, and to the role played by the charges left on the active areas of the dielectric surface or in the gas gap above it [34]. Several models have been proposed in the literature for simulating microdischarge generation, evolution and quenching, even in non uniform electric field configurations. Unfortunately, they are limited, due to numerical constraints, to single-microdischarge events [35–40]. Thus, more experimental and analytical studies are needed for their general assessment and validation.

The paper is organized as follows. In Section 2, we briefly review the state of the art on SDBD. In Section 3, we describe the experimental set up, and in Section 4, we present the plasma diagnostics employed, the latter consisting of a Rogowski coil (Section 4.1) and a photomultiplier (Section 4.2). The experimental results are discussed in Section 5, and the conclusions are summarized in Section 6.

2. Recent Works on SDBD Microdischarges

The study of the SDBD microdischarges is an active field of research which has drawn a great deal of interest in recent years, both in applied and basic plasma physics communities. We briefly review some of the works relevant for our present study.

In [41], the authors studied an extension of SDBD to a volume-surface dielectric barrier discharge for the ozone production and benzene degradation. Concerning the discharge characterization, they found that both SDBD and V-SDBD configurations worked in a filamentary discharge mode, which produced current pulses superimposed to the capacitive current, resulting in an increasing number and amplitude of current pulses with the applied voltage. In a typical SDBD configuration, the charges are transferred along a thin layer on the dielectric surface, and the accumulation of charges on the dielectric surface finally leads to a reduction in the transfer, and therefore to the extinction of the electric discharge. Compared to conventional SDBD, the hybrid volume-surface DBD (V-SDBD) apparently enhances the discharge current, widening the spatial distribution of discharge plasma, which can be explained by the enhanced spatial electric field due to the added ground electrode over SDBD configuration.

In [42], the inactivation of *Bacillus subtilis* spores using coplanar surface dielectric barrier discharge (CSDBD) is studied. As in any other plasma-chemical application, the efficacy of the treatment depends on various discharge operating conditions, such as discharge electrode geometry, mean dissipated power, and feed gas flow and composition, all of which influence the chemical and physical processes of the discharge. For that reason, the authors studied the plasma properties using a photomultiplier and ICCD camera to record the optical emission waveforms and the spectra collected from the whole surface of the CSDBD electrode. The production of micro-discharges occurs with a certain distribution along the rising slope of a positive half-period with a typical pulse-to-pulse separation of a few microseconds. A similar trend can be observed during any negative halfcycle. The characteristic distribution of micro-discharges during both the positive and negative half-cycles captured by the photomultiplier tube (PMT) waveforms for a (peak-to-peak) HV amplitude of 22 kV, has been acquired by averaging over 1024 samples. The highest probability of micro-discharge onset occurs for positive AC voltages between 6.6 and 7 kV, while for negative AC voltages, the best conditions occur between −8.5 and −9.5 kV. Further insight can be obtained by analysing the voltage, current and PMT waveforms for micro-discharges onset at a defined HV amplitude.

In [43], the effects of optical characteristics, electrical performances and mechanical properties of SDBD carrying a composite dielectric glass/polyimide film were investigated. The current, discharge plasma morphology, electrical power consumption, and induced airflow velocity were analyzed at an applied voltage of 17–23 kV with a working frequency of 9.15 kHz. The SDBD physical process of discharge is complicated, of which discharge characteristics are influenced by many factors, including the applied power, electrode parameters, dielectric properties, environmental conditions and so on. The discharge intensity at the positive half cycle is higher than the negative one, corresponding to a large number of intense pulses with noticeable amplitude difference, and the maximum pulse current peak is about 17 mA. The changes in current are relatively low, having an average value of about 4 mA during the negative half cycle.

3. Plasma Device Setup

The configuration adopted in our experiments was suggested by the simplest version of SDBD used in plasma aerodynamics applications, named a plasma actuator [18]. It consists of two conducting electrodes attached at the opposite sides of a flat dielectric panel, in the asymmetrical arrangement sketched in Figure 2.

The lower electrode is fully covered with an insulating material, whereas the upper one remains fully exposed to the air. In this way, the plasma generation region is confined above the dielectric plate. As a dielectric barrier, we used a teflon sheet with a thickness of about 3 mm.

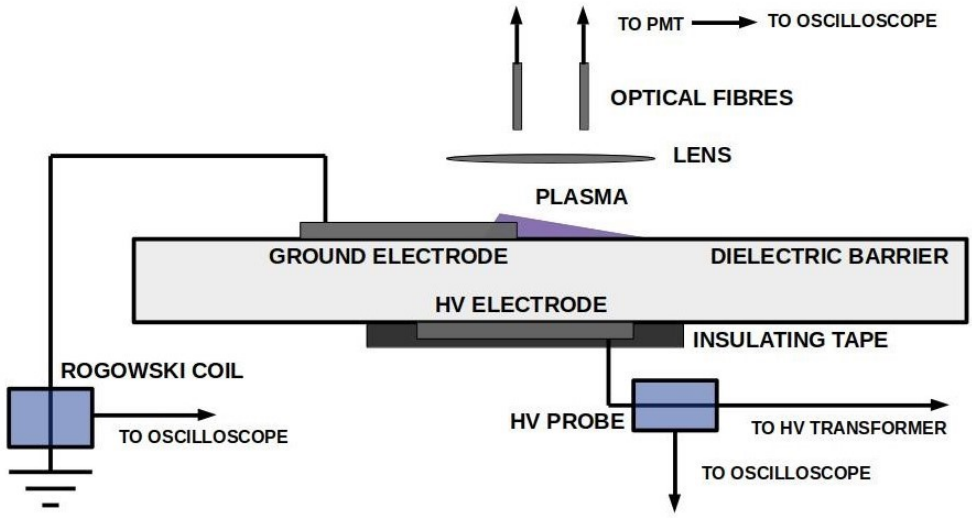

Figure 2. Plasma device scheme: the two electrodes, consisting of tin clad copper adhesive tapes (60 µm thick, 4 cm wide and 12 cm long), are attached to a dielectric material and are laterally shifted from each other by about 0.5 cm (typical asymmetry in SDBD). The lower electrode, fed by the high-volatage (HV) supply, is covered with an insulating material, whereas the upper one, fed to ground, is exposed to air (second type of asymmetry). The Rogowski coil is placed around the ground cable and it is linked to an oscilloscope. The optical fibres are placed over the plasma region (violet colour) and are connected to the photomultiplier, the latter linked to an oscilloscope. The HV probe is net to the oscilloscope from the HV cable. In this work, unless otherwise specified, an asymmetric SDBD refers to the second type of asymmetry.

Upon the application of a sufficiently high-voltage (HV), the air portion in proximity of the device gets weakly ionized, thus creating a thin plasma layer above the insulating plate, as illustrated in Figure 2. The SDBD plasma actuator generates a non-thermal self-limiting plasma in which the accumulation of charged particles onto the dielectric surface opposes the applied electric field [20]. Consequently, AC or pulsed high-voltages are required to have a temporally prolonged discharge operation, otherwise only a transient air ionization occurs at the voltage ignition [6].

In the present configuration, the exposed electrode is grounded, whereas the covered one is fed by a high-voltage power supply line. This consists of a DC-voltage supply and a signal generator feeding the primary windings of a HV transformer whose secondary windings are connected to the electrode. We set the reference DC-supply voltage, V_{DC}, in the small range, V_{DC} = (7–14) V. The whole system behaves like a resonant circuit, so the sinusoidal voltage frequency slightly depends on the DC-supply voltage. In Figure 3a, we report the coupling of the applied DC voltage and the resulting amplified HV. In Figure 3b, a typical high-voltage response signal used in the experiments is reported.

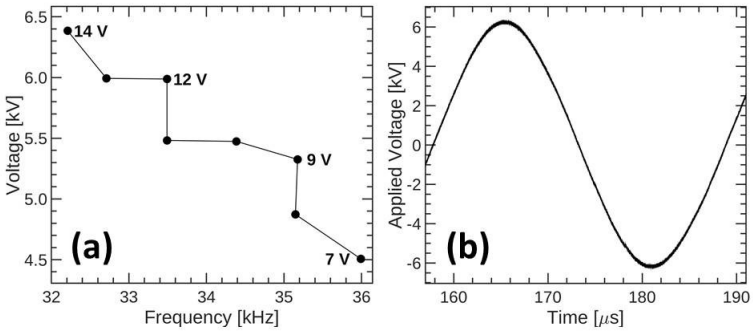

Figure 3. (**a**) Amplitude of the amplified voltage V_{HV}, resulting from the applied reference DC voltage, V_{DC} (of which few values are indicated), as a function of the corresponding optimal frequency. The latter is chosen to maximize the output voltage V_{HV}, for each reference value V_{DC}. (**b**) Typical applied signal $V_{HV}(t)$ vs. time, employed in our experiments.

4. Plasma Diagnostics

The experimental setup consists of a Rogowski coil to investigate the electrical parameters of the discharges, and an optical emission spectroscopy and photomultiplier tube to investigate the electromagnetic radiation of the plasma emission.

4.1. Rogowski Coil

The electrical parameters involved in the discharge events are clearly the most relevant to be measured. This includes the sampling of the instantaneous value of the voltage, as close as possible to the exposed electrode. Since a direct measure of the electric field or potential in the discharge region is generally not feasible, because of the perturbations it induces, the second leg of this diagnostics system is a measurement of the instantaneous value of the current flowing between the electrodes. In our experiments, this was done by means of Rogowski coil sensors [44,45].

A Rogowski coil usually consists of a conductor winding wrapped around a toroidal support of a non-ferromagnetic material, such as an air core. This ensures excellent linearity to the response of the coil due to the absence of saturation and fast timing sensitivity. To use a Rogowski coil as a probe, the cable transporting the current has to pass through the toroid. Then, the current flowing in the cable generates a voltage variation at the output of the coil proportional to the rate of the current variation, $\mathrm{d}I/\mathrm{d}t$. This voltage signal should be passed through an integrating circuit, that could simply be a resistance, for measuring $I(t)$. Using a small resistance for the integrating system, the probe operates in the so called self-integrating mode in a large frequency range.

Within this range, the voltage signal produced by the coil is directly proportional to the instantaneous current value. Outside this range, however, the probe response displays a frequency-dependent attenuation and phase-shift. Thus, in order to recover the actual value of the current, an accurate calibration and a FFT decomposition of the signal is required [45]. There are some difficulties related to air core Rogowski coils, such as the variation of the coil parameters with temperature and the sensitivity to the exact location and orientation of the circuit section passing through the torus. However, the main drawbacks in our application are due to the fact that Rogowski coils with air core have small sensitivity to

weak currents. This cannot be overlooked, since our aim is to identify the signal produced by single microdischarges.

To overcome this problem, a ferromagnetic coil can be employed for the Rogowski coil core. Here, we use NiZn ferrite N30 with $\mu_i \sim 4300$, with 50 Ω integration resistance and 3.5 windings, and a 50 cm-long RG-59 BNC coaxial cable with a 50 Ω resistance, which were calibrated with our Rogowski coil. Data were digitized by an Agilent Infinium MSO8104A oscilloscope with 1 GHz bandwidth and maximum acquisition rate of 4 GSamples/sec, which was found to be suitable for the applications we envisaged.

The electric current signal sampled by the Rogowski coil has two main components: the first one consists of the microdischarges producing the plasma state, and the second one is due to the displacement current within the insulated electrode as a result of the HV applied voltage. Thus, for a time-dependent applied voltage, a displacement current is always added to the actual discharge current flow, that is mainly determined by the capacitance behavior of the electrode system. In the case of an oscillating voltage supply, the displacement current has a sinusoidal trend with the same frequency as the applied bias.

Above a voltage threshold, the electric field ignites the plasma. This is generally observable as a pulsed current signal that overlaps the displacement current signal, consisting of several fast spikes (bursts), yielding two well-separated half-cycle patterns within the HV cycle. Since we are only interested in the plasma contribution, we chose the self-integrating range of the probe so that it suppresses the low frequency capacitive component by itself.

The calibration of the circuit was performed by using frequency waveform generators, depending on the frequency range to be analyzed. We used an NF-1940 Synthesizer, with bandwidth (0–20) MHz, and a Kenwood SG-7130 Synthesizer, with bandwidth (0.1–1300) MHz. The Rogowski coil was inserted using two BNC breakouts, as close as possible to a high-power 50 Ω resistor R (Bird Electronic Co. 8135, maximum power 150 W) in order to avoid the external cable stray capacitances. We collected input HV probe signal and Rogowski output signal through an oscilloscope. Using the amplitude attenuation and phase-shift information, we obtained the calibration parameters shown in Figure 4. Unless otherwise stated, we referred to the phase during the oscillation cycle as the argumentof a sine function expressed in radiants, such as

$$V_{\mathrm{Rog}}(t) = V_{\mathrm{Rog}} \sin(\omega t + \phi_{\mathrm{Rog}}). \tag{1}$$

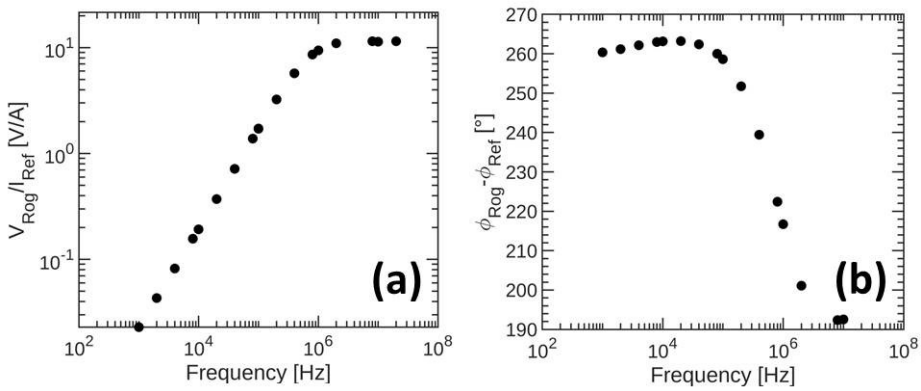

Figure 4. Calibration of the Rogowski coil vs. frequency [Hz]. (**a**) Voltage response. (**b**) Phase shift.

After the amplitude calibration, we obtained the attenuation factor to correct our Rogowski response in the bandwidth (10^6–10^8) Hz, which is fit to measure the characteristics of current pulses corresponding to single individual microdischarges, i.e.,

$$\frac{V_{\mathrm{Rog}}}{I_{\mathrm{Ref}}} \sim 10\ \mathrm{V/A}, \tag{2}$$

where I_{Ref} is the reference current in the frequency range (10^6–10^8) Hz. This is the self-integrating bandwidth that we extrapolate up to 10^9 Hz. Using this optimised design of the coil, a phase calibration correction [45] is no longer needed.

4.2. Photomultiplier Tube

As is well known, during the development of an electrical discharge, part of the energy is lost into the excitation of internal states of atoms and molecules. From their de-excitation, plasma emissions of electromagnetic radiation are produced, and part of this radiation lies in the optical range. This could be exploited for diagnostics purposes by using optical emission spectroscopy (OES) [46]. In addition to providing information on the emitting species, the time of emission could give some hints about the mechanisms of the discharge itself. This is all the more true for SDBD, where the region of emission is concentrated and discharge happens mainly through quick, independent events of ionization and subsequent electric current flow, when most of the excitations happens [6,23]. The spreading and development of the discharge in the air gap can then be traced by registering the delays in the emissions.

Here, we use a multi-anode PMT (Hamamatsu H8711), built upon 16 channels arranged in a 4×4 matrix form. Each channel can collect electrons coming from a 4.3 mm square photocathode. The rise time of the PMT signal, 0.83 ns, is short enough to retain the relevant information of the emitting times. Their high sensitivity is optimal to obtain light even from single discharge events. In our experiments, we kept the gain of the PMT constant, by supplying it with a regulated high-voltage generator (Matsusada AU-5R20-LCl), biased to −850 V.

Besides having suitable rise time and multichannels, the choice of the PMT was motivated also by the radiant sensitivity of the photocathode, a bialkali one, in order to match with the plasma emission spectrum. The model we use has a maximum sensitivity in the 300–500 nm range. This fits well the reported average discharge emission spectra, measured in the range 200–850 nm by means of a wide-band and low-resolution spectrometer (PS2000 by Ocean Optics), similar to those already discussed in [23]. They are consistent with typical spectra of dielectric barrier discharges in air at atmospheric pressure, with the brightest feature being the second positive system of molecular nitrogen N_2, approximately lying in the interval 300–500 nm, and showing minor evidence of the first negative system of the nitrogen molecular ion N_2^+, extending to the 380–480 nm range. One such spectrum is shown in Figure 5, together with the sensitivity curve of the PMT.

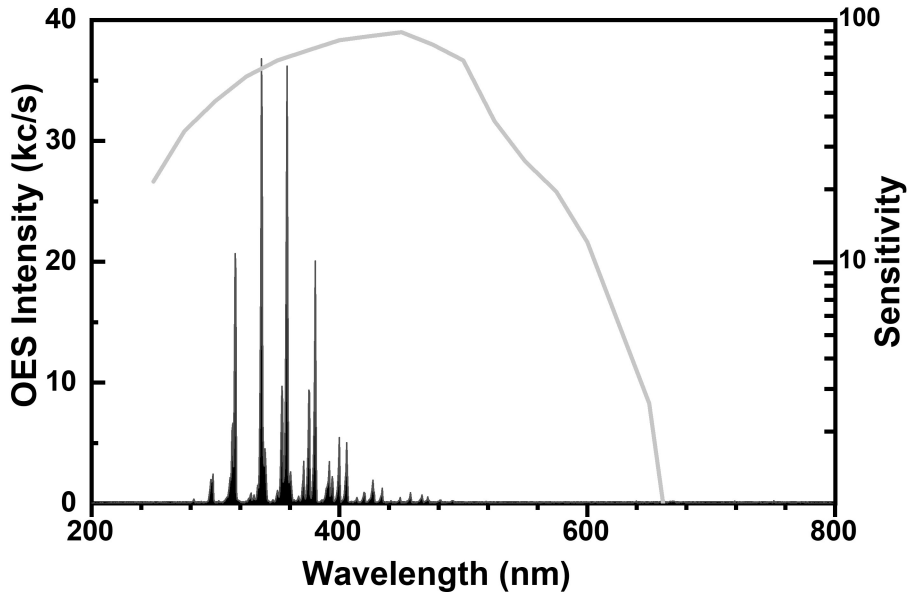

Figure 5. Light emission spectra of a typical discharge recorded by a low resolution spectrometer, compared to the sensitivity range of the photomultiplier tube (PMT) (continuous line).

The radiative lifetime of the excited levels involved in the emission of the second positive system is around 40 ns. However, quenching in atmospheric air, enhanced also by impurities and excited states produced in the plasma gas-phase, reduces the lifetime of such excited levels to below 1 ns. Thus, the sensitivity of the excitation timing is retained and OES could be used to measure the spatio-temporal development of the discharges [47]. This was the main goal of our OES measurements.

The outputs of the PMT were registered on the low impedance input (50 Ω) of a fast digital scope (Agilent MSO-8104Al). This retains the timing information of the emission, while producing pulses which could easily be recorded and separated from the noise. Usually, the light emitted from each microdischarge appears in the recorded temporal series as a (3 ± 1) ns negative voltage pulse, which is due to the temporal response of our PMT. Indeed, the signals were absolutely similar to those detected when collecting light emitted by a lamp. The shape of the signal could also be used to safely remove electromagnetic disturbances occasionally coming from the discharge.

The light emitted from plasma microdischarges was collected by UV-enhanced optical fibres by Avantes (FCB-UV800-2). In order to increase light collection, instead of placing the optical fibres directly above the discharge region, we imaged the discharge onto their inlets by means of a commercial objective lens (1:2.8/F = 50 mm by Durst). In the simplest OES setup, we chose to look first at two spatially separated spots. By back-illuminating the optical fibres, we could check the actual size and location of the discharge region imaged by each of the channels of the PMT. Since we are primarily interested in the correlations and delays between plasma emission from different discharge regions, we should exclude any spurious signal arising from cross-talk between the different channels of the PMT. This was indeed one of main factors in the choice of the PMT.

As an example, we show in Figure 6 a portion of the time series recorded by the digital scope, where a couple of light pulses associated to plasma microdischarges are detected by a channel of the multianode PMT. Besides the shape of the pulses, it appears that no signal was associated to the second channel (in this case, we chose two pins at the opposite corners of the square PMT matrix), where the optical fiber input was plugged in. We also tested that all channels are similar in sensitivity and time response, and switched the viewlines several times in order to exclude any interference from the choice of the PMT channels.

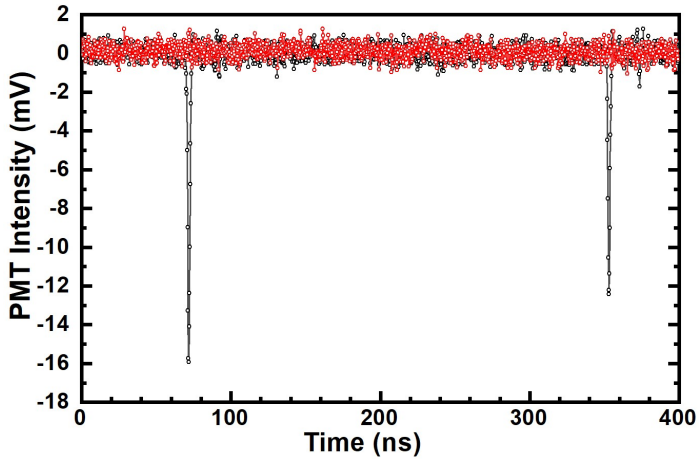

Figure 6. PMT output recorded by two different channels, the black one looking at the discharge and the red one blinded, showing the shape of the signals (vertical lines) coming from the plasma and the absence of cross-talk.

5. Experimental Results

In the following, we discuss the experimental results for the Rogowski coil measurements in Section 5.1, and for the PMT measurements in Section 5.2.

5.1. Rogowski Coil

Every oscilloscope channel acquisition has 41×10^6 points, sampled every 0.25 ns. That means that every acquisition length is 1.025 ms. To increase the statistics, we analyzed 30 realizations for each voltage, yielding a total time span of 30.75 ms. A typical one-cycle signal acquisition is plotted in Figure 7a, where the left axis refers to the applied voltage (black line) and the right axis refers to the current measured by the Rogowski coil (red line).

When the applied voltage $V > 0$, the electrons go from the exposed electrode to the dielectric, and the current is defined as negative. The discharges that occur in this case are denoted as a forward stroke (FS). The discharges that occur in the opposite condition, $V < 0$, are denoted as a backward stroke (BS), and have an associated current defined as positive. For this reason, if a spike is positive (negative) in a forward (backward) stroke, it is classified as noise. We also consider as noise a peak that both develops within 25 ns after a burst and has a height lower than 75% of the previous burst. These spurious signals are due to the finite system bandwidth.

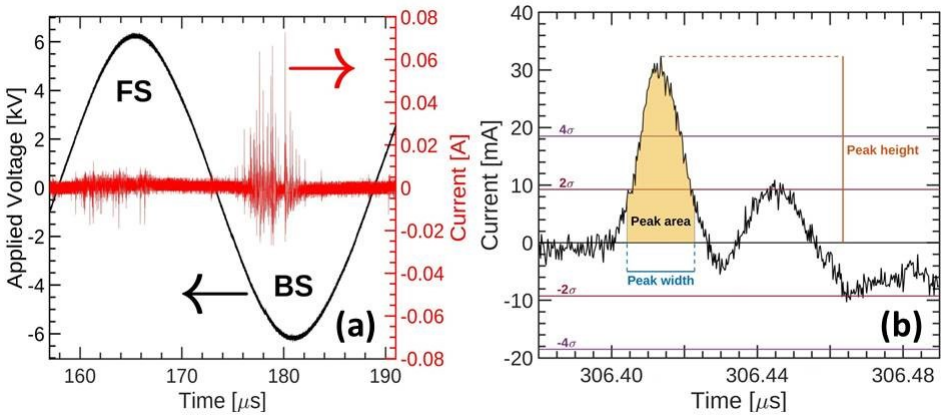

Figure 7. (**a**) Example of a temporal acquisition (forward stroke (FS) when $V > 0$, and backward stroke (BS) when $V < 0$). The left axis refers to the applied voltage (black line), while the right axis refers to the Rogowski coil current (red line). (**b**) Burst (peak) properties: charge (peak area), maximum current (peak height), and temporal duration (peak width).

We performed a fit of the HV signal with a sine function to determine its amplitude, frequency, and argument at each point. From the current signal, we can notice the presence of a constant baseline and a series of spikes that occur at specific HV phases. These spikes are the current signal caused by the plasma microdischarges. Detail of a microdischarge (called burst) is shown in Figure 7b. We characterize a burst by its charge (area of the peak), maximum current intensity (height), time duration (width), and HV phase position. Since we are interested only in the plasma current, carried by the bursts, we have to determine a background threshold above which a peak can be defined as a burst. We choose as background threshold, $\epsilon_B = 2\sigma$, i.e., twice the standard deviation over the whole Rogowski coil data. We identify a peak as a burst if its height is greater than the value of 4σ. The peak duration is given by the peak width at ϵ_B.

5.1.1. Phase Analysis

We determine first the normalized burst count distribution as a function of phase within a single HV cycle (Figure 8). One can notice two well-separated phase zones. The FS occurs at lower phases $0 \leq \phi \leq \pi$, and the BS when $\pi \leq \phi \leq 2\pi$. The number of events within FS is much smaller than within BS. It can be noted that for BS, the number of bursts increases with increasing HV, and a double peak structure emerges at high HV. The origin of this structure remains to be understood.

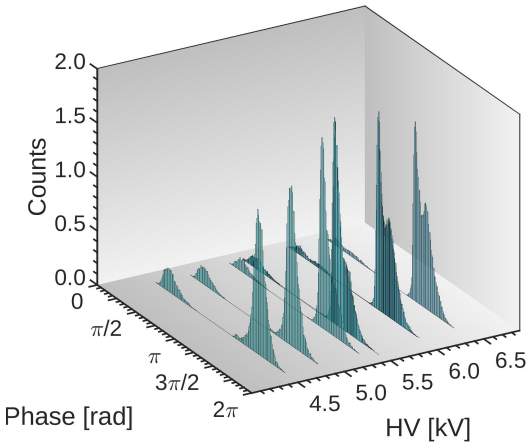

Figure 8. Distribution of bursts counts vs. HV phase. The FS occurs for phases $0 \leq \phi \leq \pi$, and the BS for $\pi \leq \phi \leq 2\pi$. Note the conspicuous difference in the counts between the FS and BS phases.

5.1.2. Charge Analysis

Next, we consider the charge Q (peak area) associated to bursts. The distributions of charge, $P(Q)$, are shown in Figure 9a for FS, and in Figure 9b for BS, respectively. The distributions are plotted in semi-logarithmic scale for clarity of presentation.

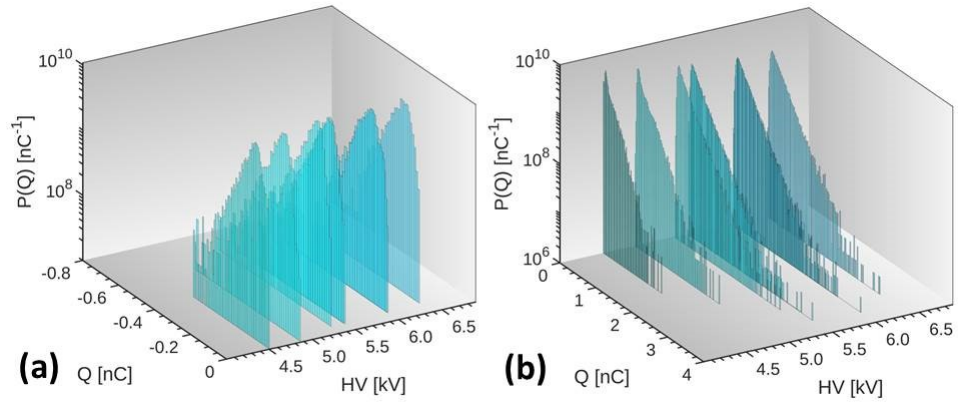

Figure 9. Burst charge distribution $P(Q)$ vs. charge Q for different HV. (**a**) Forward stroke (negative charge). (**b**) Backward stroke (positive charge).

For a more quantitative analysis, we consider the charge distribution $P(Q)$ for a single HV, in the illustrative case HV = 5.48 kV, shown in Figure 10. The two half-cycle responses, the FS and BS, are plotted for comparison. Both distributions display a maximum near $Q = 0$, while for BS, the decay is approximately exponential at large Q.

Thus, for BS we use the exponential form to fit the charge distributions,

$$P(Q) = \frac{1}{Q_0} \exp\left(-\frac{Q}{Q_0}\right), \tag{3}$$

where Q_0 is a characteristic charge. The values of Q_0 are shown in Figure 11a, as a function of the applied HV. As one can see, the characteristic charge Q_0 first increases with HV, reaching a plateau for HV larger than $\simeq 5.4$ kV. The latter can be seen as the separation voltage between two different regimes, similar to that found for DBD [26]. The plateau value $Q_0 \simeq 0.7$ nC suggests that BS bursts reach a maximum saturation charge at high voltages.

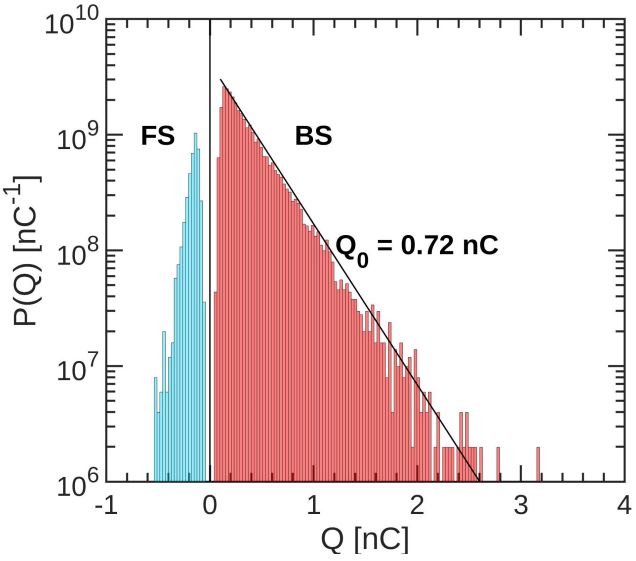

Figure 10. Distribution $P(Q)$ vs. Q for both FS ($Q < 0$) and BS ($Q > 0$) at HV = 5.48 kV. For BS, we find the exponential decay $P(Q) \simeq \exp(-Q/Q_0)$, for $Q > 0$, with $Q_0 \simeq 0.72$ nC.

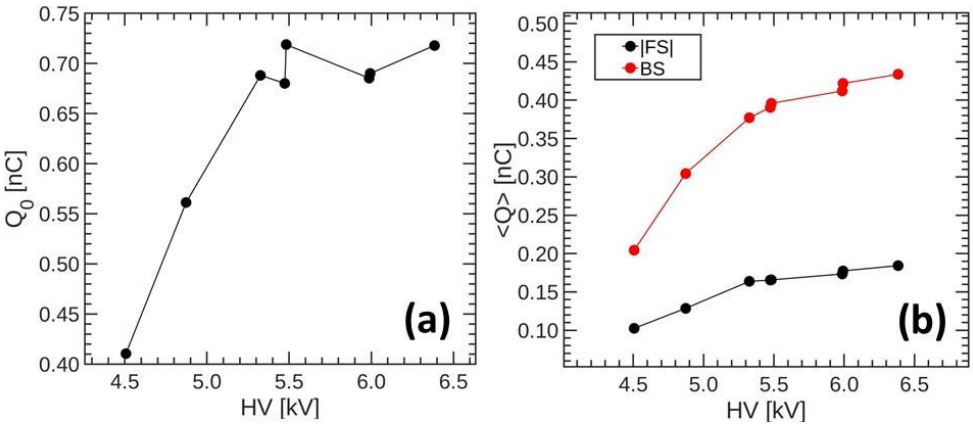

Figure 11. (**a**) Characteristic charge Q_0 vs. HV for BS. (**b**) Mean charge $\langle |Q| \rangle$ for both FS and BS.

The corresponding mean charges, $\langle |Q| \rangle$, are shown in Figure 11b. The mean charge (absolute) values are very different, ∼0.35 nC for BS and ∼(−)0.15 nC for FS. This asymmetry, both in the number and charge of bursts, is consistent with the existence of different discharge mechanisms due to the setup asymmetry.

5.1.3. Burst Time Duration Analysis

Let us consider next the distribution of burst time duration (see Figure 12).

As is apparent from Figure 12, the distributions $P(\tau)$ are asymmetric and their shapes are non-Gaussian. Indeed, there occur a large number of events of long duration, as the skewness and the flatness (also known as kurtosis) testify. The skewness is a measure of the asymmetry of the distribution around its mean value ($S_\tau = 0$ for a normal distribution), and the flatness is a measure of the relative importance of the values at the tails ($F_\tau = 3$ for the normal distribution). The corresponding moments, S and F, for the actual burst distribution strongly differ from their Gaussian counterparts, as one can see in Figure 13. Furthermore, for BS, the mean duration of bursts increases with the applied voltage and is about $\langle \tau \rangle \simeq 15$ ns for HV=5.5 kV; for FS, $\langle \tau \rangle \simeq 11$ ns, and it is weakly dependent on HV.

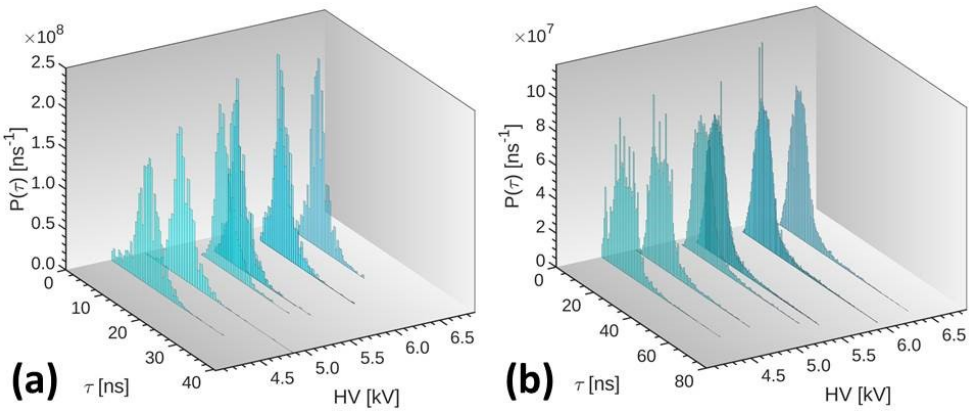

Figure 12. Burst time duration distribution, $P(\tau)$ vs. τ, for different HV. (**a**) Forward stroke. (**b**) Backward stroke. Note the different time scales in (**a**,**b**).

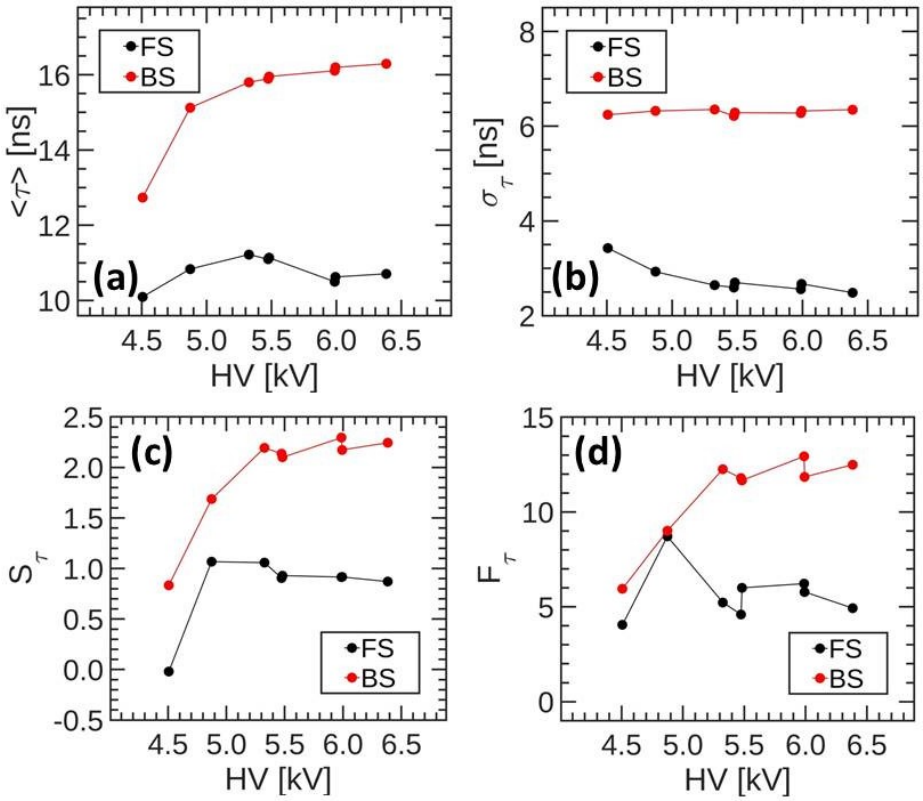

Figure 13. Moments of burst time duration vs. HV. (**a**) Mean value $\langle\tau\rangle$. (**b**) Standard deviation σ_τ. (**c**) Skewness (S_τ). (**d**) Flatness (F_τ).

5.1.4. Current Analysis

The burst current distributions, $P(I)$, display an exponential shape similar to $P(Q)$. For BS, the current distributions are shown in Figure 14. To describe the current distributions for BS, we assume an exponential shape for $P(I)$, as we did for $P(Q)$, Equation (3), $P(I) = (1/I_0)\exp(-I/I_0)$.

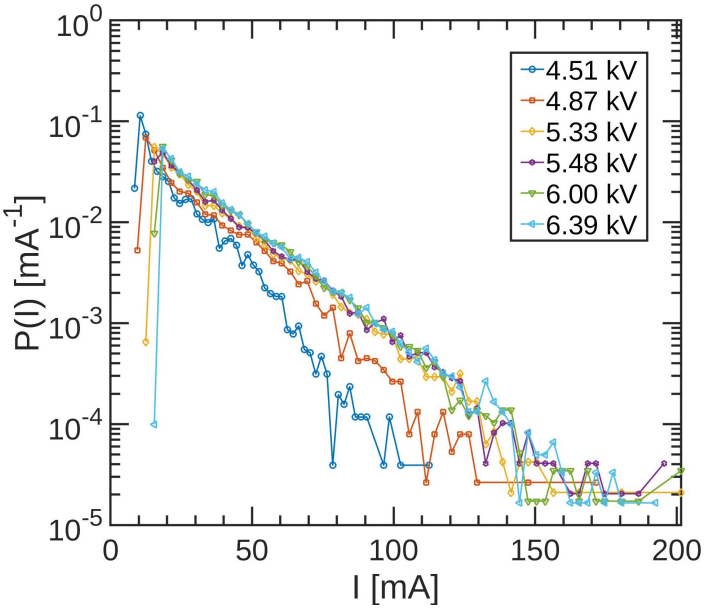

Figure 14. The BS current distribution, $P(I)$ [mA^{-1}] I [mA], for different HV, displaying a shape which is approximately exponential at the tails.

The values of the characteristic currents I_0 are reported in Figure 15a. This behaviour can be compared with a similar HV dependence found for Q_0 in Figure 11. A plateau above about 5.4 kV is also observed here for the characteristic current I_0. Finally, the mean values of the current, $\langle I \rangle$, are displayed in Figure 15b, where one can see that for BS, the mean currents are much larger than for FS. For example, at HV = 5.5 kV, $\langle I \rangle \sim 35$ mA for BS, while $\langle I \rangle \sim (-)20$ mA for FS.

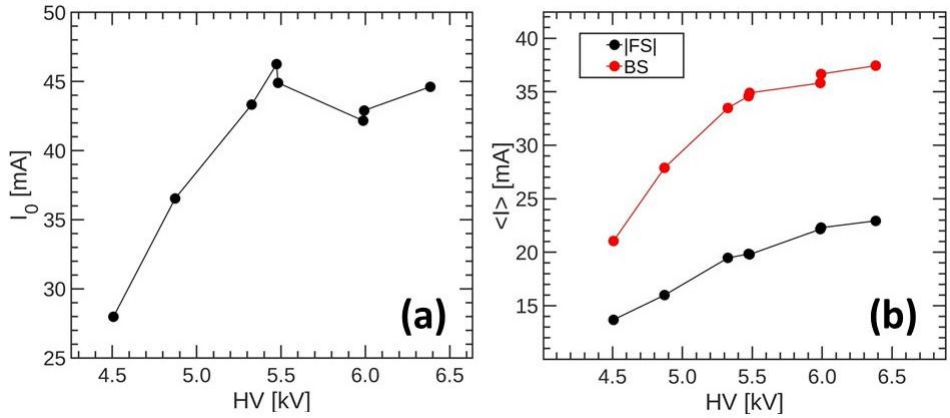

Figure 15. (**a**) Characteristic current I_0 [mA] and (**b**) mean current $\langle I \rangle$ [mA] vs. HV [kV].

Analogously to the moments shown in Figure 13, we report in Figure 16 the corresponding ones for the burst current. They definitively show that the associated distributions are also non-Gaussian.

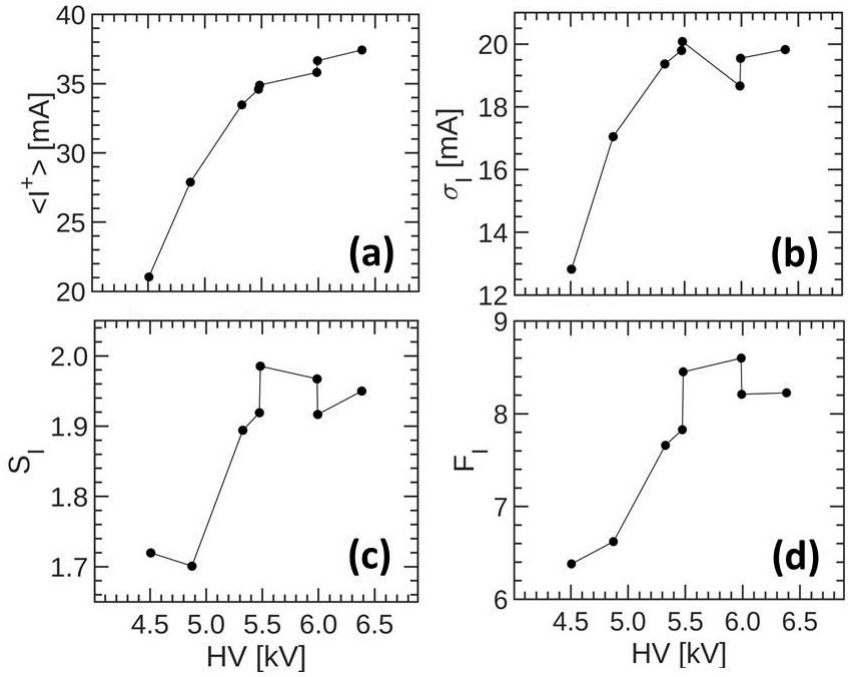

Figure 16. Same as in Figure 13 for the BS currents. Note that the value HV $\simeq$ 5.5 kV seems to play the role of a separation voltage between two regimes, as found for the charge.

5.1.5. Correlations between BS

A question that often arises in DBD is whether bumps (here called strokes) are correlated to each other [26]. The same quest applies to our SDBD results. We therefore calculated, for our records, the cross-correlations, $C^{(i,j)}_{BS,BS}$, between BS separated by a time lag $\Delta t = |i-j|T$, where T is the applied signal period, according to the standard definition,

$$C^{(i,j)}_{BS,BS} = \frac{\left\langle [I^{(i)}_{BS}(t) - \langle I^{(i)}_{BS}\rangle][I^{(j)}_{BS}(t) - \langle I^{(j)}_{BS}\rangle]\right\rangle_{\Delta t}}{\sigma^{(i)}_{BS}\sigma^{(j)}_{BS}}, \tag{4}$$

where $I^{(i)}_{BS}(t)(>0)$ is the value of the burst current within the ith BS at time t, $\langle I^{(i)}_{BS}\rangle$ the mean current value, and $\sigma^{(i)}_{BS}$ the corresponding standard deviation.

A typical cross-correlation analysis is illustrated in Figure 17, for HV = 5.48 kV. Similar results (not shown here) are obtained for the other applied voltages. As one can see from this analysis, there is a residual or almost no apparent temporal correlations between BS.

Therefore, in order to uncover a possible hidden structure of BS, we compared two consecutive BS with each other (i.e., 1–2, 3–4, etc.), by building their burst current intensity differences as a function of time,

$$\Delta I^{(i+1,i)}_{BS,BS}(t) = I^{(i+1)}_{BS}(t) - I^{(i)}_{BS}(t), \tag{5}$$

for $i = 1, 3, 5, \ldots, 2N_p - 1$, where N_p is the total number of consecutive BS pairs in the record. An example is shown in Figure 18a, for $i = 1$ and HV = 5.48 kV. As one can see, bursts do not occur at the same time (note that the time origin, the start of the BS half-cycle, is the same for all strokes). We found that the time delay between bursts follows a uniform random distribution (results not shown).

Next, to find the mean behaviour of BS, we average the differences in Equation (5), determined at fixed times $t = n\Delta$, with $1 \le n \le N$ and $\Delta t = 0.25$ ns, over all pairs N_p,

$$\left\langle \Delta I^{(i+1,i)}_{BS,BS}(t)\right\rangle_i = \frac{1}{N_p}\sum_{j=1}^{N_p} \Delta I^{(2j,2j-1)}_{BS,BS}(t). \tag{6}$$

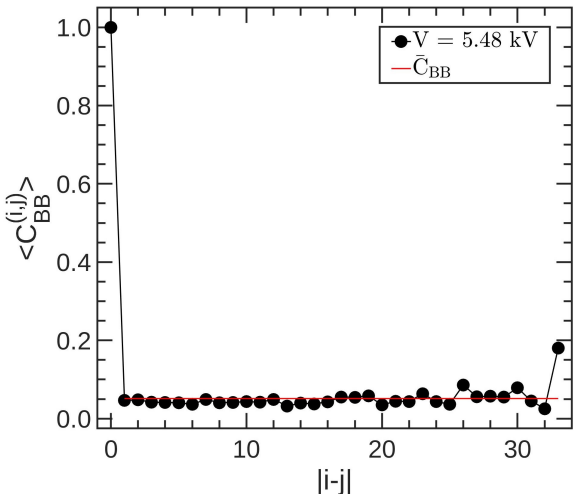

Figure 17. Mean cross-correlations between bumps as time lag for $V = 5.48$ kV.

The mean differences are plotted in Figure 18b, where one can see that they do not average out to zero. To better visualize the evolution of differences, it is convenient to add them sequentially, as follows

$$S(n) = \sum_{j=1}^{n} \left\langle \Delta I^{(i+1,i)}_{BS,BS}(j\Delta t) \right\rangle_i. \tag{7}$$

Their time behavior can be conveniently visualized by adding the differences sequentially as for random walks (red line in the figure). The corresponding random walk (RW) profiles, for selected applied HV, are displayed in Figure 19a.

In order to determine the degree of auto-correlation in the signal, in this case referred to a sequence of two consecutive BS, we rely on the calculation of the Hurst exponent (see e.g., [26,32,33]). To this end, we evaluate the mth ($1 \leq m \leq N/\ell$) mean RW profile at 'time scale' ℓ ($\ell \equiv t/\Delta t$), with $1 \leq \ell \leq N$, given by

$$B_m(\ell) = \frac{1}{\ell} \sum_{n=1}^{\ell} S[(m-1)\ell + n]. \tag{8}$$

Next, we study the fluctuations between neighboring boxes according to,

$$F(\ell) = \left\langle [B_{m+1}(\ell) - B_m(\ell)]^2 \right\rangle^{1/2}, \tag{9}$$

which is expected to display a power-law behaviour,

$$F(\ell) \simeq \ell^H, \tag{10}$$

where $0 \leq H \leq 1$. It should be noted that fully uncorrelated RW has $H = 1/2$, and $H = 1$ for fully correlated ones. The results shown in Figure 19b suggest that initially, within about 6 ns, the neighboring BS remain strongly correlated. A second regime develops at intermediate times, $6 < t < 200$ ns, suggesting that weaker correlations persist and are well described by an exponent $H \simeq 2/3$. This behaviour is consistent with a temporal fractal-like regime in which discharge fluctuations show self-similar properties. Finally, above about 200 ns, fluctuations tend to remain constant due to the finite duration of the signal, and fluctuations cannot develop further.

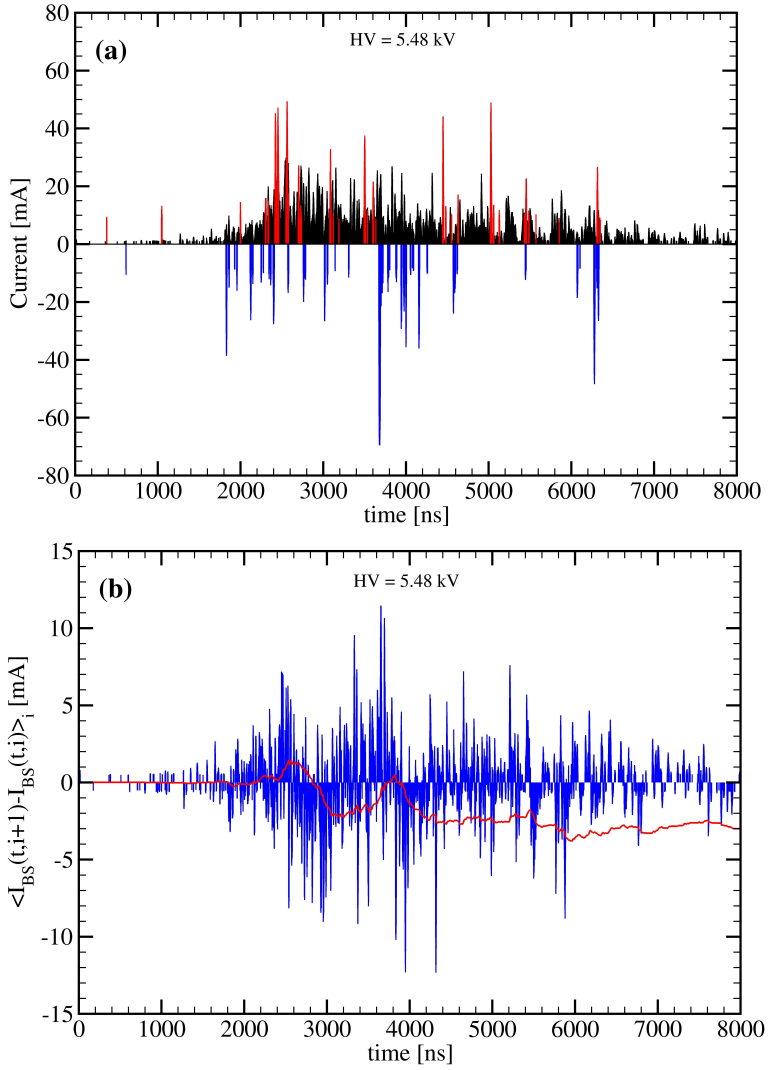

Figure 18. Internal structure of BS. (**a**) The second BS (red vertical lines), compared with the first one ($i = 1$) (blue vertical lines), the latter multiplied by -1 in order to directly visualize their differences, for the applied voltage HV = 5.48 kV. The black vertical lines represent the mean backward stroke (shown as a reference), obtained by averaging BS over the whole record (in this case 34 half-cycles). The time origin coincides with the start of the BS half-cycle, and therefore it is the same for all strokes. (**b**) Mean current differences, Equation (6), between consecutive BS (blue vertical lines). The accumulated mean differences, $S(n)$, with $n = t/\Delta t$ Equation (7), behave as a random walk time profile (red line).

5.2. Photomultiplier Results

The fast time response of PMT allows us to employ optical diagnostics to study the temporal evolution of the discharge pattern and evaluating the differences between FS and BS. In particular, the use of a multi-anode PMT allows us to measure the correlations and the delays in the plasma light emission between different regions above the active dielectric surface.

In the following, we report results from the analysis of the emitting times of light measured with photomultiplier tubes (PMT) [48]. In particular, we focus on the measurements of the direction and velocity of propagation of light emission along the insulating barrier surface. This was achieved by simultaneously collecting light coming from different points of the discharge air gap.

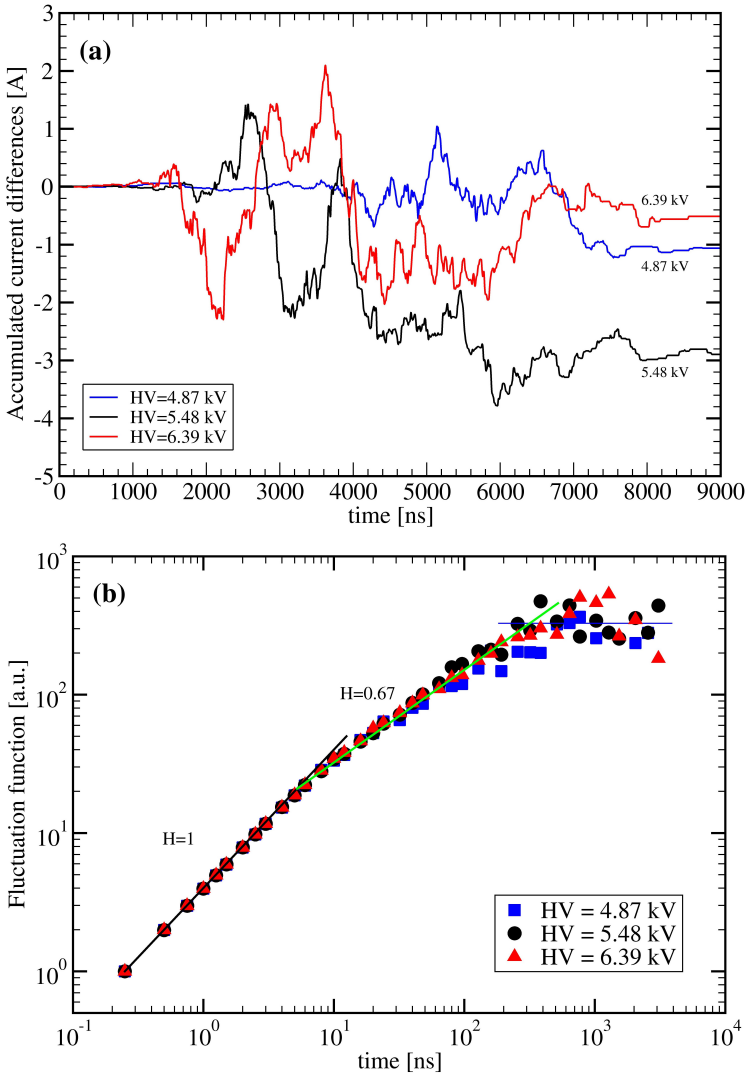

Figure 19. Analysis of time correlations between BS. (**a**) Accumulated mean current differences (random walk profiles) between successive BS for different HV. (**b**) Hurst exponent analysis of fluctuations for the profiles shown in (**a**). The values $H = 1$, for times $t < 6$ ns, and $H = 0.67$, for intermediate times 6 ns $< t <$ 200 ns, represent the slopes of the black and green straight lines, respectively.

First, we locate the position of the bulk of the plasma emission. The discharges are well confined within a thin air sheet of one−two millimeters above the dielectric surface, next to the exposed electrode edge (see Figure 20). Discharges occur where the electric field, determined by the applied external high voltage signal, is maximal. Plasma emissivity is concentrated on such edge and expands for a few millimeters above the dielectric surface, whereas its extension above the exposed electrode is much more limited [23]. The actual size of the active optical region does depend, although not strongly, on the applied high voltage, also increasing in the late phases of the strokes. This is of use to look for correlations and delays in the light emission along the dielectric surface.

It should be noted that the plasma emissivity is quite uniform, on average, in the direction parallel to the exposed electrode edge, until the lateral edges (see Figure 20). Indeed, we did not observe significant differences between different portions of the exposed electrode edge. Moreover, we did not observe any significant correlation in the light emission times from regions even a few millimeters apart along the electrode edge direction. This implies that each discharge event develops mainly in the direction perpendicular to the electrode edge and its lateral extension is limited, as well as its height on the dielectric surface. This

confirms also that each discharge event, identified by current bursts, evolves independently from the others, even when partial overlapping in time happens.

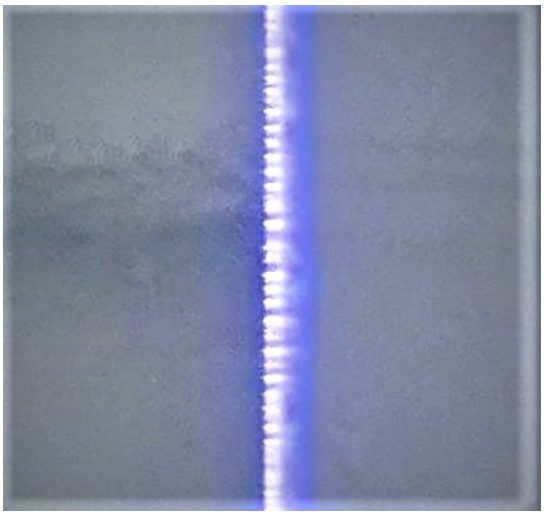

Figure 20. Plasma discharges observed in our SDBD for $V = 5.48$ kV.

The most interesting findings were, however, observed when the PMT channels collected light from regions aligned along a direction perpendicular to the exposed electrode edge. Here, correlation in light emission could be observed, and also delays between the light emission timing could be measured. When light is detected by the PMT on one of its channels, we observe a burst in the corresponding time series, as in Figure 6. Occasionally, we detect several bursts, sometimes partially overlapping, with a global duration which generally never exceeds 10 ns. These events, although interesting, were excluded from the analysis. Light detected in the first channel arrives from a region just across the edge of the exposed electrode, whereas the second channel samples a spot (each about 800 µm in diameter) 2.5 mm away on the dielectric surface.

We find that the detected bursts appear to be very similar in the two channels, with average amplitudes, respectively, of 22.9 ± 0.9 and 21.8 ± 0.9 mV and durations, respectively, of 3.71 ± 0.08 and 3.62 ± 0.09 ns. Their average numbers are different, unveiling the lower emissivity of the regions above the dielectric surface as one moves away from the electrode edge. Over a sample of about one thousand oscillations, the counting rate of bursts is, for the two channels, 130 ± 11 and 74 ± 8 kHz, of which about 65% was within the BS. Another interesting behaviour was found by looking at the times, and the HV phases, when light emission occurred. Although emissivity is somewhat stable over different oscillations, it shows a detectable and characteristic distribution during each HV cycle [48]. In both space regions, emissivity in the BS phase concentrates around the breakdown time and shows a second maximum later on.

On the contrary, emission within a FS is more uniformly distributed with the different phases of the HV oscillation. Another interesting feature of the optical emission pattern is linked to its persistency. Although about half of the events are accompanied by at least another during the same half-cycle, but only a slight minority (less than 10%); this second one is nearer than 250 ns, and in the other case the next one happens in the following half-cycle (about 40%) or in the subsequent cycle. In only 0.5% or 3% of the events, respectively, above the electrode edge and on the dielectric surface, no light was detected in the two subsequent half-cycles. This means that the spatial pattern of the discharges stays more or less stable over a relevant number of subsequent strokes and that the discharges belonging to each half-cycle are spatially related. Moreover, as a path of discharge is established, this repeats over the same spatial location, even if the timing (and so the external electric field strength) could be quite different from one event to the subsequent one. This memory effect is probably related to the dynamics of ions after the microdischarge quenching and

in particular to the charging of the dielectric surface, which could explain the persistance of the discharge pattern between subsequent HV cycles.

Finally, we compare the results of the emitting times between the two PMT channels. Now, all PMT bursts are ordered in time and the minimum delay between bursts belonging to a couple of different channels are calculated. A histogram of estimated delays can thus be obtained, and it is shown in Figure 21 [48].

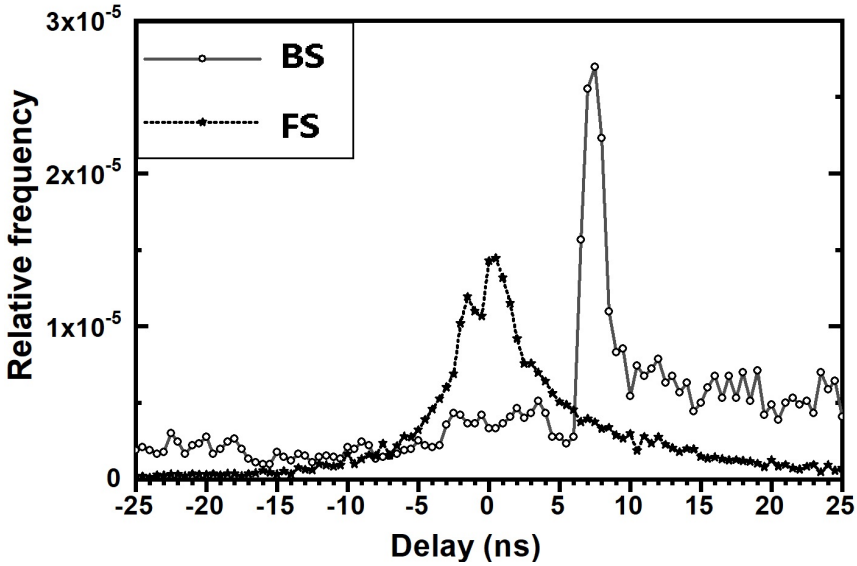

Figure 21. Distribution of delays between bursts in the forward (stars) and backward (o) strokes.

A quite evident maximum appears in BS, corresponding to an average delay of 8.4 $\pm$ 1.6 ns. This implies a propagation of the ionizaing wave from the electrode edge to the dielectric surface, with an average rate of about 300 km/s. Such propagation occurs in the direction opposite to that of the electron drift, dictated by the external electrode voltage and compatible with a cathode directed streamer mechanism of discharge [2,48].

Nothing comparable could be revealed by the analysis of the FS delays. In this case, the distribution is quite symmetrical, with a slight prevalence of the positive delays. It is also significantly larger and peaking at almost zero delay. It looks like as if propagation happens on a faster time scale, that cannot be revealed by the emission timing alone and with a significant spread. Because of the small sample and uniformity of distribution with the HV phase, FS events do not show any significant dependence of the delay either on the applied HV nor on its instantaneous value.

In the case of BS, it is easy to separate bursts belonging to the near breakdown phase from the group happening towards the maximum HV amplitude. However, the distribution of delays continues to show a single defined burst, with almost the same delay, with only slight differences in the relative height and its tails. This implies that the ionizing wave propagation is not strongly dependent on the actual phase or the absolute value of the external electric field, being somewhat controlled by the local conditions developing with the microdischarge itself. This is in broad agreement with the properties reported for the microdischarges themselves, as discussed previously.

6. Conclusions

We have reported results on the statistical properties of asymmetric surface dielectric barrier discharges with an exposed metal electrode, and the other fully isolated from air, both glued onto a dielectric surface. We study the charge, current, and duration of the individual discharge events composing the two active phases of the SDBD, denoted as forward and backward strokes (FS and BS), respectively. A strong asymmetry between the two strokes has been found. For the BS, the mean charge carried by a burst is about 0.3 nC, the mean current

is 35 mA and the duration is 15 ns, while for the FS, the corresponding values are smaller in magnitude—that is, −0.1 nC, −20 mA and 11 ns, respectively.

We have studied temporal correlations between two successive backward strokes, by building the random walk profiles resulting from differences in current discharges evaluated at the same time within the BS cycle. We applied a fluctuation analysis to extract the scaling behavior of the profiles at different times scales. We found a well defined power-law of fluctuations, for 6 ns $< t <$ 200 ns, characterized by a Hurst exponent $H \sim 2/3$, suggesting the presence of persistent (positive) correlations between consecutive BS. At times $t <$ 6 ns, the correlation is maximal, leading to $H = 1$. The correlations found at intermediate times are a result of non-trivial phenomena related to the interaction between discharges and plasma. These findings should be useful for better assessing the models attempting to describe this complex behaviour.

We have also measured the optical emission of discharges using a photomultiplier to further study spatial correlation patterns. The optical emission is produced by electron impact excitations due to the ionizing wave propagation igniting the discharge. In particular, we have measured the spreading rate of the ionizing wave associated to microdischarges for BS. The wave moves, mostly perpendicularly, away from the edge of the exposed electrode towards the dielectric surface, roughly corresponding to the direction of the electric field determined by the instantaneous voltage level applied to the insulated electrode, but opposite to the electron drift motion. This is also the direction of the produced ionic wind. Both the order of magnitude and the direction of the ionizing wave velocity are compatible with a cathode directed streamer mechanism. However, the absence of a corresponding propagation for the microdischarges for FS points towards the presence of a different mechanism acting in this opposite phase.

Author Contributions: Conceptualization, C.R. and C.P.; methodology, C.R., R.B., C.P; software, R.B.; validation, C.P., R.B.; formal analysis, C.P., R.B., H.E.R.; investigation, C.P.; resources, C.R.; data curation, C.P.; writing—original draft preparation, C.P., R.B., H.E.R.; writing—review and editing, C.P., H.E.R.; visualization, C.P.; supervision, C.R.; project administration, C.R.; funding acquisition, C.R. All authors have read and agreed to the published version of the manuscript.

Funding: This research received no external funding.

Acknowledgments: We gratefully acknowledge the technical support of Alessandro Mietner in the device development and experiment execution.

Conflicts of Interest: The authors declare no conflict of interest.

Abbreviations

The following abbreviations are used in this manuscript:

DBD	Dielectric barrier discharge
SDBD	Surface dielectric barrier discharge
UV	Ultraviolet
FS	Forward stroke
BS	Backward stroke
AC	Alternating current
HV	High voltage
DC	Direct current
FFT	Fast Fourier transform
OES	Optical emission spectroscopy
PMT	Photomultiplier tube
RW	Random walk

References

1. Eliasson, B.; Kogelschatz, U. Modeling and applications of silent discharge plasmas. *IEEE Trans. Plasma Sci.* **1991**, *19*, 309–323. [CrossRef]
2. Raizer, Y.P. *Gas Discharge Physics*; Springer: Berlin/Heidelberg, Germany, 1991.

3. Kogelschatz, U. Filamentary, patterned, and diffuse barrier discharges. *IEEE Trans. Plasma Sci.* **2002**, *30*, 1400–1408. [CrossRef]
4. Becker, K.H.; Kogelschatz, U.; Schoenbach, K.H.; Barker, R. *Non-Equilibrium Air Plasmas at Atmospheric Pressure*; CRC Press: Boca Raton, FL, USA, 2004.
5. Fridman, A.; Kennedy, L.A. *Plasma Physics and Engineering*; CRC Press: Boca Raton, FL, USA, 2004.
6. Kogelschatz, U. Dielectric-barrier discharges: Their history, discharge physics, and industrial applications. *Plasma Chem. Plasma Process.* **2003**, *23*, 1–46. [CrossRef]
7. Brandenburg, R. Dielectric barrier discharges: Progress on plasma sources and on the understanding of regimes and single filaments. *Plasma Sources Sci. Technol.* **2017**, *26*, 053001. [CrossRef]
8. Fridman, A.; Chirokov, A.; Gutsol, A. Non-thermal atmospheric pressure discharges. *J. Phys. Appl. Phys.* **2005**, *38*, R1. [CrossRef]
9. Esena, P.; Zanini, S.; Riccardi, C. Plasma processing for surface optical modifications of PET films. *Vacuum* **2007**, *82*, 232. [CrossRef]
10. Zanini, S.; Grimoldi, E.; Citterio, A.; Riccardi, C. Characterization of atmospheric pressure plasma treated pure cashmere and wool/cashmere textiles: Treatment in air/water vapor mixture. *Appl. Surf. Sci.* **2015**, *349*, 235. [CrossRef]
11. Napartovich, A.P. Overview of atmospheric pressure discharges producing nonthermal plasma. *Plasmas Polym.* **2001**, *6*, 1–14. [CrossRef]
12. Siliprandi, R.; Zanini, S.; Grimoldi, E.; Fumagalli, F.; Barni, R.; Riccardi, C. Atmospheric pressure plasma discharge for polysiloxane thin films deposition and comparison with low pressure process. *Plasma Chem. Plasma Process.* **2011**, *31*, 353–372. [CrossRef]
13. Massines, F.; Gherardi, N.; Sommer, F. Silane-based coatings on polypropylene, deposited by atmospheric pressure glow discharge plasmas. *Plasmas Polym.* **2000**, *5*, 151–172. [CrossRef]
14. Zanini, S.; Citterio, A.; Leonardi, G.; Riccardi, C. Characterization of atmospheric pressure plasma treated wool/cashmere textiles: Treatment in nitrogen. *Appl. Surf. Sci.* **2018**, *427*, 90. [CrossRef]
15. Zanini, S.; Freti, S.; Citterio, A.; Riccardi, C. Characterization of hydro- and oleo-repellent pure cashmere and wool/nylon textiles obtained by atmospheric pressure plasma pre-treatment and coating with a fluorocarbon resin. *Surf. Coat. Technol.* **2016**, *292*, 155. [CrossRef]
16. Dell'Orto, E.C; Vaccaro, A.; Riccardi, C. Morphological and chemical analysis of PP film treated by Dielectric Barrier Discharge (Conference Paper). *J. Phys. Conf. Ser.* **2014**, *550*, 012032.
17. Barni, R.; Riccardi, C. Perspective of NOx removal from numerical simulation of non-thermal atmospheric pressure plasma chemical kinetics. *High Temp. Mater. Process.* **2010**, *14*, 205.
18. Corke, T.C.; Post, M.C.; Orlov, D.M. SDBD plasma enhanced aerodynamics: Concepts, optimization and applications. *Prog. Aerosp. Sci.* **2007**, *43*, 193–217. [CrossRef]
19. Enloe, C.L.; McLaughlin, T.E.; VanDyken, R.D.; Kachner, K.D.; Jumper, E.J.; Corke, T.C. Mechanisms and responses of a single dielectric barrier plasma actuator: Plasma morphology. *AIAA J.* **2004**, *42*, 589–594. [CrossRef]
20. Pons, J.; Moreau, E.; Touchard, G. Asymmetric surface dielectric barrier discharge in air at atmospheric pressure: Electrical properties and induced airflow characteristics. *J. Phys. Appl. Phys.* **2005**, *38*, 3635. [CrossRef]
21. Caruana, D. Plasmas for aerodynamic control. *Plasma Phys. Control. Fusion* **2010**, *52*, 124045. [CrossRef]
22. Corke, T.C.; Enloe, C.L.; Wilkinson, S.P. Dielectric barrier discharge plasma actuators for flow control. *Annu. Rev. Fluid Mech.* **2010**, *42*, 505–529. [CrossRef]
23. Biganzoli, I.; Barni, R.; Riccardi, C.; Gurioli, A.; Pertile, R. Optical and electrical characterization of a surface dielectric barrier discharge plasma actuator. *Plasma Sources Sci. Technol.* **2013**, *22*, 025009. [CrossRef]
24. Roth, J.R.; Sherman, D.M.; Wilkinson, S.P. Electrohydrodynamic flow control with a glow-discharge surface plasma. *AIAA J.* **2000**, *38*, 1166–1172. [CrossRef]
25. Post, M.L.; Corke, T.C. Separation control on high angle of attack airfoil using plasma actuators. *AIAA J.* **2004**, *42*, 2177–2184. [CrossRef]
26. Siliprandi, R.A.; Roman, H.E.; Barni, R.; Riccardi, C. Characterization of the streamer regime in dielectric barrier discharges. *J. Appl. Phys.* **2008**, *104*, 063309. [CrossRef]
27. Orlov, D.M.; Font, G.I.; Edelstein, D. Characterization of discharge modes of plasma actuators. *AIAA J.* **2008**, *46*, 3142–3148. [CrossRef]
28. Dedrick, J.; Boswell, R.W.; Audier, P.; Rabat, H.; Hong, D.; Charles, C. Plasma propagation of a 13.56 MHz asymmetric surface barrier discharge in atmospheric pressure air. *J. Phys. Appl. Phys.* **2011**, *44*, 205202. [CrossRef]
29. Biganzoli, I.; Barni, R.; Gurioli, A.; Pertile, R.; Riccardi, C. Experimental investigation of filamentary and non-filamentary regimes in a surface dielectric barrier plasma actuator. *J. Phys. Conf. Ser.* **2014**, *550*, 012038. [CrossRef]
30. Biganzoli, I.; Barni, R.; Riccardi, C. Temporal evolution of a surface dielectric barrier discharge for different groups of plasma microdischarges. *J. Phys. Appl. Phys.* **2012**, *46*, 025201. [CrossRef]
31. Raizer, Y.P.; Mokrov, M.S. Physical mechanisms of self-organization and formation of current patterns in gas discharges of the Townsend and glow types. *Phys. Plasmas* **2013**, *20*, 1091604. [CrossRef]
32. Koscielny-Bunde, E.; Bunde, A.; Havlin, S.; Roman, H.E.; Goldreich, Y.; Schellnhuber, H.-J. Indication of a universal persistence law governing atmospheric variability. *Phys. Rev. Lett.* **1998**, *81*, 729. [CrossRef]
33. Kantelhardt, J.W.; Roman, H.E.; Greiner, M. Discrete wavelet approach to multifractality. *Phys. Stat. Mech. Its Appl.* **1995**, *220*, 219–238. [CrossRef]

34. Barni, R.; Biganzoli, I.; Dell'Orto, E.C.; Riccardi, C. Effect of duty-cycles on the air plasma gas-phase of dielectric barrier discharges. *J. Appl. Phys.* **2015**, *118*, 143301. [CrossRef]
35. Unfer, T.; Boeuf, J.P. Modeling and comparison of sinusoidal and nanosecond pulsed surface dielectric barrier discharges for flow control. *Plasma Phys. Control. Fusion* **2010**, *52*, 124019. [CrossRef]
36. Likhanskii, A.V.; Shneider, M.N.; Macheret, S.O.; Miles, R.B. Modeling of dielectric barrier discharge plasma actuator in air. *J. Appl. Phys.* **2008**, *103*, 053305. [CrossRef]
37. Hoskinson, A.R.; Hershkowitz, N. Modelling of dielectric barrier discharge plasma actuators with thick electrodes. *J. Phys. Appl. Phys.* **2011**, *44*, 085202. [CrossRef]
38. Nishida, H.; Abe, T. Numerical analysis of plasma evolution on dielectric barrier discharge plasma actuator. *J. Appl. Phys.* **2011**, *110*, 013302. [CrossRef]
39. Barni, R.; Esena, P.; Riccardi, C. Chemical kinetics simulation for atmospheric pressure air plasmas in a streamer regime. *J. Appl. Phys.* **2005**, *97*, 073301. [CrossRef]
40. Shang, J.S.; Huang, P.G. Surface plasma actuators modeling for flow control. *Prog. Aerosp. Sci.* **2014**, *67*, 29–50. [CrossRef]
41. Shang, K.; Wang, M.; Peng, B.; Li, J.; Lu, N.; Wu, Y. Characterization of a novel volume-surface DBD reactor: Discharge characteristics, ozone production and benzene degradation. *J. Phys. Appl. Phys.* **2019**, *53*, 065201. [CrossRef]
42. Doležalová, E.; Prukner, V.; Kuzminova, A.; Simek, M. On the inactivation of Bacillus subtilis spores by surface streamer discharge in humid air caused by reactive species. *J. Phys. Appl. Phys.* **2020**, *53*, 245203. [CrossRef]
43. Wei, W.; He, S.; Yang, Z.; Wang, S.; Mei, G.; Gao, G.; Wu, G. Electromechanical efficiency improvement of the surface DBD by composite dielectric. *AIP Adv.* **2019**, *9*, 045127. [CrossRef]
44. Argüeso, M.; Robles, G.; Sanz, J. Implementation of a Rogowski coil for the measurement of partial discharges. *Rev. Sci. Instrum.* **2005**, *76*, 065107. [CrossRef]
45. Biganzoli, I.; Barni, R.; Riccardi, C. Note: On the use of Rogowski coils as current probes for atmospheric pressure dielectric barrier discharges. *Rev. Sci. Instrum.* **2013**, *84*, 016101. [CrossRef] [PubMed]
46. Laux, C.O.; Spence, T.G.; Kruger, C.H.; Zare, R.N. Optical diagnostics of atmospheric pressure air plasmas. *Plasma Sources Sci. Technol.* **2003**, *12*, 125. [CrossRef]
47. Hoder, T.; Brandenburg, R.; Basner, R.; Weltmann, K.-D.; Kozlov, K.V.; Wagner, H.-E. A comparative study of three different types of barrier discharges in air at atmospheric pressure by cross-correlation spectroscopy. *J. Phys. Appl. Phys.* **2010**, *43*, 124009. [CrossRef]
48. Barni, R.; Biganzoli, I.; Riccardi, C. Spatial and temporal evolution of microdischarges in Surface Dielectric Barrier Discharges for aeronautical applications plasmas. *J. Phys. Conf. Ser.* **2014**, *550*, 012036. [CrossRef]